Construction and Properties of Ag-I Polymeric Clusters Attach with Nitrogen Heterocyclic Transition Metal Moiety

Min Liu[1] · Yu Xin[1] · Yong Heng Xing[1] · Feng Ying Bai[1] · Zhan Shi[2]

Abstract
Two silver cluster compounds $\{[Co(1,10'-phen)_3]_2 \cdot [Ag_8I_{12}]\}$ (**1**) and $\{[Co(2, 2'-bipy)_3] \cdot [Ag_{10}I_{11}] \cdot (OH) \cdot 3DMF \cdot 2H_2O\}$ (**2**) $(1,10'-phen = 1,10'-phenanthroline, 2, 2'-bipy = 2,2'-bipyridine)$ were designed and synthesized by solvent evaporation method. The two silver cluster compounds were characterized by elemental analysis, infrared spectroscopy, ultraviolet spectroscopy, thermogravimetric analysis and X-ray powder diffraction. The crystal structures of compounds **1** and **2** were determined by X-ray crystallography diffraction. Through the electrostatic interaction between the metallic Ag cluster moiety and the metallic Co cluster moiety, form stable interlaced layered super molecular structures. In order to explore functional properties, the catalytic reduction of p-nitrophenol (PNP) and electrochemical behavior of compounds **1** and **2** were explored. The results show that compounds **1** and **2** can efficiently catalyze the reduction of PNP in the aqueous solution, and the reduction and removal rate can reach more than 90%.

Graphical Abstract
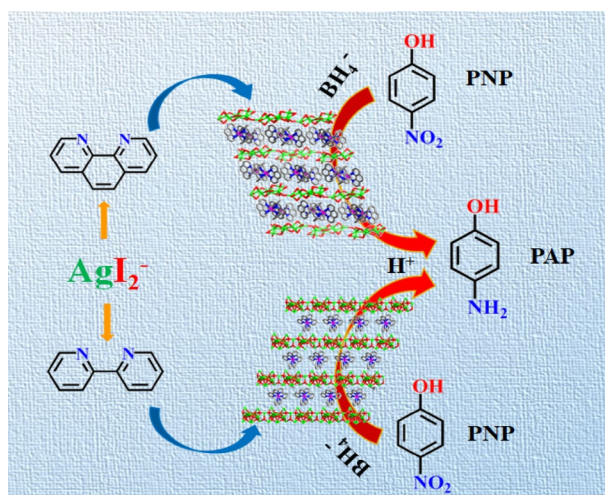
Keywords Silver cluster compounds · Electrochemistry · P-nitrophenol · Catalytic

✉ Yong Heng Xing
  xingyongheng2000@163.com

✉ Feng Ying Bai
  baifengying2003@163.com

Extended author information available on the last page of the article

1 Introduction

Nowadays, with the rapid development of industry, agriculture, and handicrafts, a large amount of hazardous organic wastewater is discharged into the water, causing water pollution, destroying the environmental balance, and even threatening human life and health. Therefore, the development of

a catalyst that can efficiently remove organic pollutants has become a current research hotspot [1, 2]. Catalytic technology is the process of degrading all the pollutants in the aqueous solution into non-toxic substances under the action of a catalyst. These compounds are usually toxic. Discharge into the water will cause water pollution and have carcinogenic effects on humans. Among the many pollutants, nitroaromatic compounds, especially nitrophenol compounds, account for a large proportion. Therefore, the removal of nitroaromatic compounds is particularly important [3–5]. So, the degradation and catalytic reduction of p-nitrophenol (PNP) and other nitrophenol compounds have attracted great attention [6–8]. As we know, PNP can be effectively reduced to p-aminophenol (PAP). PAP is an effective industrial intermediate, which can be used in analgesic and antipyretic drugs, imaging agents, antiseptic lubricants, etc. In 2016, Sá et al. used molecular hydrogen as a reducing agent for the first time to produce PAP by continuous flow hydrogenation of PNP. This method is to convert a toxic substance into another non-toxic product through an oxidation–reduction reaction, and the by-product is only water, and water is also a solvent, which provides a new idea for removing PNP [9]. In 2016, Zhu et al. used Ni-Ca-Al$_2$O$_3$ to catalyze the reduction of PNP. The mechanism is that Ni-Ca-Al$_2$O$_3$ catalyzes the release of H$_2$ from NaBH$_4$, and then reduces PNP to PAP [10]. In 2019, Chen et al. synthesized W-TiO$_2$/SiO$_2$ catalyst and studied that it can photo catalyze PNP with a mineralization rate of about 99%. PNP is first degraded into intermediates by light, and these intermediates are further degraded into smaller fragments such as organic carboxylic acids, and finally fully mineralized [11]. It can be seen that catalytic technology is widely used in the treatment of organic pollutants, and its removal effect is also significant. In 2020, Feng et al. used nano-pyrite to catalytically reduce PNP. Nano-pyrite is dissolved to release Fe^{2+} under acidic conditions, and then H$_2$O$_2$ is added. H$_2$O$_2$ produces a large amount of ●OH under the action of Fe^{2+}, and finally ·OH catalyzes reduction of PNP to produce CO$_2$ and H$_2$O [12]. Eshaq et al. prepared a core–shell nanostructure FeVO$_4$@CeO$_2$, which was used as a catalyst to achieve the catalytic reduction and degradation of PNP [13]. Catalytic hydrogenation is a method in which NaBH$_4$, H$_2$O or C$_2$H$_5$OH is used as a hydrogen donor to provide active hydrogen for the catalytic process, and then the aromatic nitro compound is catalytically reduced to an aromatic amino compound [14–17]. In 2020, Shimoga et al. studied the mechanism of silver nanoparticles (SNPs) catalyzing the PNP process: After sodium borohydride aqueous solution interacts with SNPs, hydrogen gas is rapidly generated and adsorbed on the surface of SNPs, thereby reducing PNP on the surface of SNPs [18]. Today, materials such as nanomaterials, graphene, metal oxides and metal organic frameworks have been used as catalysts for the catalytic reduction of PNP [19–21]. Among

them, the metal–organic framework has the characteristics of high surface area, high porosity, high stability, etc., which has attracted wide attention. Therefore, looking for an efficient metal–organic framework catalyst has become one of the future research directions.

Nitrogen heterocyclic complexes are metal organic frameworks with specific structures formed by using nitrogen heterocyclic organic compounds as ligands and connecting with the central metal. A simple nitrogen heterocyclic ring is an organic compound containing a five-membered or six-membered heterocyclic structure in the molecule, which means that there is at least one nitrogen atom in the heterocyclic ring [22]. Nitrogen heterocyclic ligands can form π-π interactions between rings to further stabilize the structure of the complex [23–27]. In 2016, Cheng et al. synthesized [{Ru(bpy)$_2$}$_3$(µ$_3$-L^2)](PF$_6$)$_6$ (bpy = 2,2'-bipyridine), and studied its photophysical and electrochemical properties [28]. In 2017, Bedowr et al. synthesized [Cu(η^1–(OOCR)$_2$(2,2'-bpy) (4,4'-bpy)] (2,2'-bpy = 2,2'-bipyridine, 4,4'-bpy = 4,4'-bipyridine), and its magnetic properties were studied [29]. In 2018, Gaml et al. synthesized the complex [Ru(bpy)$_2$(Hapbim)]$^{2+}$ (bpy = 2,2'-bipyridine, Hapbim is 2-aminophenylbenzimidazole), and measured it by spectrophotometry Optical properties [30]. In 2019, Doyle et al. synthesized {[Hphen][Fe(phen)(H$_2$P$_2$O$_7$)$_2$]·2H$_2$O} (phen = 1,10′-phenanthroline) and studied its magnetic properties [31]. Yakhvarov et al. synthesized new nickel phosphate complexes [Ni(HPO$_4$)(bpy)$_2$] (bpy = 2,2'-bipyridine) and [Ni(HPO$_4$)(phen)$_2$]. The X-ray crystal structure analysis of the complexes showed that the nickel ions have a twisted octahedral complex. The complex structure and diverse functions of silver clusters have attracted wide attention [32]. In 2016, An et al. used the fluorescence enhancement of the silver nanocluster complex to efficiently detect calcium ion [33]. In 2017, Zang et al. connected the silver cluster complexes to adaptable ligands to connect them to each other and form a rigid metal–organic framework. Multicolor lights made of volatile organic compounds that are triggered off by oxygen [34]. In 2018, Liang et al. stated in a review that several silver complexes have antibacterial, antifungal, anticancer and other biological activities [35]. In 2020, Weng et al. designed a thermally fluorescent color-changing elastic polymer film by incorporating silver nanoclusters. The color of the polymer film changes when the temperature is higher than 120 ℃, and the fluorescence was enhanced [36]. In 2020, Xue et al. synthesized two compounds {[Cr(DMSO)$_6$][Ag$_6$I$_9$]·H$_2$O} and {[Ni(DMSO)$_6$][Ag$_5$I$_7$]}, compounds possesses photodegradation activity and recyclability toward methyl violet, and studied photocatalytic mechanisms for compounds [37]. In 2021, Pan et al. report a *dia*-type metal–organic hybrid network based on the [Ag$_4$Br$_6$] clusters and hexamethylenetetramine molecules, the complex presents a dual emission and exhibits
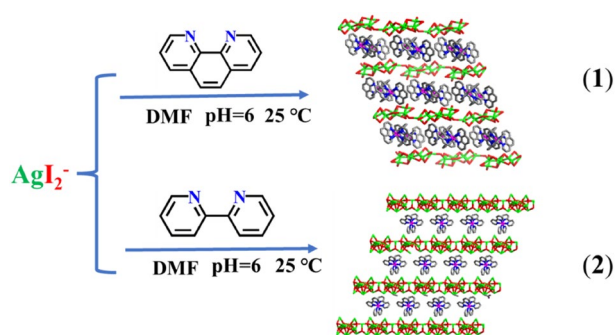
Scheme 1 The synthetic routes of **1** and **2**

luminescent thermochromism behavior [38]. In 2021, Lu et al. synthesized Ag/Au clusters by reacting the π-acidic cyclic trinuclear Ag(I) pyrazolate and its Au(I) analogue with 3-substituted phenylacetylene, the Ag/Au clusters exhibit high-energy phosphorescence tunable from blue to cyan through the modulation of the substituents on the phenylacetylene ligand [39]. At present, the silver cluster compounds are still under continuous research.

Therefore, two silver cluster compounds {[Co(1, 10′-phen)_3]_2·[Ag_8I_{12}]} (**1**) and {[Co(2,2-bipy)_3]·[Ag_{10}I_{11}]·(OH)·3DMF·2H_2O} (**2**) were designed and synthesized based on 1, 10′-phenanthroline and 2, 2′-bipyridine ligands by solvent evaporation method, the electrochemical behavior of **1** and **2** and the optimal resting time, pH and sweep rate of the cyclic voltammetry curve were studied. The catalytic reduction of PNP was also explored, and the catalytic reduction of PNP was also investigated. The mechanism of the process was speculated, the reduction and removal rate can reach more than 90%.

2 Experimental

2.1 Materials and Method

All chemicals purchased were of reagent grade or better and were used without further purification. Solvents were purified according to the standard methods. The instrument used in this work is in the supporting information.

2.2 Preparation of 1 and 2

In this work, 1,10′-phenanthroline and 2,2′-bipyridine were used as ligands, AgI_2^- was used as the metal source, and the silver cluster compounds **1** and **2** was synthesized by solvent volatilization under the conditions of DMF solvent [40]. The detailed preparation methods of **1** and **2** were described in the supporting information. The synthetic route for the compounds **1** and **2** were summarized in Scheme 1.

2.3 Fabrication of Electrodes

The BCPE was made by 0.75 g of graphite powder and 0.25 g of paraffin wax. Mixed the two evenly, after 3 times of heating and grinding, put them into a self-made glass tube with a diameter of 3 mm, and finally insert a copper wire [41, 42]. The same process to prepare the working electrode. During the grinding, add 10 mg of the compound was added to the carbon paste.

Cyclic voltammetry uses a three-electrode system: the reference electrode is a saturated calomel electrode, the counter electrode is a platinum electrode, the working electrode is a carbon paste electrode, and the electrolyte solution is a 1 M KCl solution. Measure cyclic voltammetry curves at different scanning speeds, different static times and different pH value [43].

2.4 Catalytic Experiment of Compounds

Add 20 mL PNP solution and 2 mL NaBH_4 solution together, the solution turns bright yellow, and then add a certain amount of compound and ultrasonic for 30 s, and measure the absorbance of the solution at a specific wavelength at different time intervals with an ultraviolet–visible spectrophotometer, calculate the reduction rate of PNP. Figure S1 was standard curve of PNP solution.

3 Results and Discussion

3.1 IR Spectra

The IR spectra of a series of the complexes were shown in Figure S2. In the IR spectrum of **1**, the characteristic peak at 1673 cm^{-1} is attributed to the C=N stretching vibration, while the C=N stretching vibration peak of the ligand 1, 10′-phen is at 1654 cm^{-1}. The C=N stretching vibration peak of **1** is red-shifted compared to the C=N stretching vibration peak of ligand 1, 10′-phen, which indicates that the metal Co(II) is coordinated with the ligand. In the IR spectrum of **2**, the vibration peak at 1663 cm^{-1} is considered to be the stretching vibration of C=N, while the C=N stretching vibration of ligand 2, 2′-bipy appears at 1665 cm^{-1}. The C=N stretching vibration of **2** is blue-shifted compared to the C=N stretching vibration peak of ligand 2, 2′-bipy, which indicates that the metal Co(II) is coordinated with the ligand. The main infrared data were listed in Table S3.

3.2 UV–Vis Spectra

The UV–Vis spectra of a series of the compounds were shown in Figure S3. The π–π* transition and n–π* transition of the ligand 1, 10′-phen appear at 256 nm and 325 nm. For

1, the two strong absorption bands at 220 nm and 308 nm were attributed to the ligand-to-ligand charge transition (LLCT). The strong absorption band at 376 nm can be attributed to the ligand-to-metal charge transition (LMCT) [44, 45]. It further shows that the metal Co(II) is coordinated with the ligand 1, 10′-phen. The two strong absorption bands at 213 nm and 309 nm are the π–π* and n–π* transitions of **2**, which can be attributed to the ligand-to-ligand charge transition (LLCT). The π–π* transition and n–π* transition of the ligand 2, 2′-bipy appear at 264 nm and 316 nm. The strong absorption band at 431 nm can be attributed to the ligand-to-metal charge transition (LMCT). It further shows that the metal Co(II) is coordinated with the ligand 2, 2′-bipy. Due to the wavelength limitation of the instrument, the characteristic absorption peak of Co is not shown. The main UV–vis spectra data were listed in Table S4.

3.3 Powder X-Ray Diffraction (PXRD)

The experimental and simulated PXRD patterns of **1** and **2** are shown in Figure S4. As shown in the Figure S4a and Figure S4b, although the peak intensity of the experimental PXRD pattern and the simulated PXRD pattern are slightly different, the positions of the respective peaks are almost the same. This indicates that **1** and **2** are pure phase without impurities. At the same time, as shown in Figure S5a and Figure S5b, the crystallinity of **1** and **2** was calculated according to the jade 5 software, which were 54.62% and 74.65%, respectively.

3.4 Thermogravimetric Analyses (TG)

To verify the thermal stability of the compound, thermogravimetric analysis was performed at a heating rate of 10 °C/min under a N_2 atmosphere with the temperature range from 30 to 800 °C. The TG curve of **1** was shown in Figure S6a, the first stage of weight loss occurs at 30–560 ℃, and the actual weight loss rate is 29.6% (theoretical weight loss rate: 30.1%), which corresponds to the loss of six 1,10′-phen ligands. The second weight loss stage occurs at 560–800 ℃, the actual weight loss rate is 8.6%, which corresponds to the collapse of the framework, and the final residue was metal oxide. The TG curve of **2** was shown in Figure S6b, the first stage of weightlessness occurs at 30–150 ℃, and the actual weight loss rate is 1.7% (theoretical weight loss rate: 1.6%), which corresponds to the loss of two water and a hydroxide ion. The second stage of weight loss occurs at 150–530 ℃, and the actual weight loss rate is 16.9% (theoretical weight loss rate: 16.0%), which corresponds to the loss of three DMF and three 2, 2′-bipy. The third weight loss stage occurs at 530–800 ℃, the actual weight loss rate is 6.0%, which corresponds to the part collapse of the framework, and the final residue was metal oxide. Comparing the weight loss of **1**

and **2**, the thermal stability of **2** is relatively better. The main thermogravimetric analyses data were listed in Table S5.

3.5 Crystal Structures of the Compounds 1 and 2

Compound **1** belongs to the monoclinic system with $P2_1/c$ space group. The molecular structure includes a metallic Ag cluster and a Co cluster dimer with six 1,10'-phen. The metal Co atom chelates with six nitrogen atoms (N1–N6) from three 1,10'-phen to form a six-coordinate octahedral configuration, as shown in Fig. 1a. The coordination mode of ligand 1, 10′-phen is μ_2-$\eta_N^1\eta_N^1$, as shown in Fig. 1c. The Ag clusters consist of eight silver ions and twelve iodide ions, as shown in Fig. 1b.

In the Ag cluster, both Ag1 and Ag2 form a deformed triangular pyramid structure, Ag1 is coordinated by two μ_2-I (I2, I8) and one μ_3-I (I3), Ag2 is coordinated by two μ_2-I (I1, I2) and one μ_3-I (I4). Among them, Ag3, Ag4, Ag5, Ag6, Ag7 and Ag8 all form a twisted tetrahedral configuration, Ag3 is coordinated by two μ_2-I (I1, I12) and two μ_3-I (I3, I5), Ag4 is coordinated by three μ_3-I (I3-I5) and one μ_4-I (I6), and Ag5 is coordinated by two μ_2-I (I7, I8), one μ_3-I (I4) and one μ_4-I (I6), Ag6 is coordinated to one μ_2-I (I10), two μ_3-I (I5, I11) and one μ_4-I (I6), Ag7 is coordinated to two μ_2-I (I7, I9), one μ_3-I (I11) and one μ_4-I (I6), Ag8 is coordinated to three μ_2-I (I9, I10, I12) and one μ_3-I (I11). The coordination environment of metallic Ag ions is shown in Table S6. The bond length range of Ag-I bond in compound **1** is about 2.709–3.252 Å, which is similar to the bond length range of Ag-I bond 2.737–3.181 Å reported in the literatures [46–48]. Six tetrahedral AgI_4 and two triangular pyramid AgI_3 are connected by sharing edges to form Ag_8I_{12} building block of Ag cluster. As shown in Fig. 1d, the Ag_8I_{12} building blocks are connected by I_{12} to form a one-dimensional chain structure. As shown in Fig. 1e and 1f, a more stable interlaced layered structure is formed between the metal Ag cluster part and the metal Co cluster part through the electrostatic interaction between the anion and the cation.

Compound **2** belongs to the monoclinic system with $C2/c$ space group. The molecular structure includes a metal Ag cluster, a metal Co cluster, a hydroxide ion, three free DMF and two lattice water. In the structure, the Co cluster is a cationic cluster with +2 valence. As shown in Fig. 2a, the metal Co atom and six nitrogen atoms from three 2, 2′-bipyridine (N1–N3, N1#1–N3#1; #1: 1 − x, y, 0.5 − z) form a six-coordinate octahedral configuration. As shown in Fig. 2c, the coordination mode of ligand 2, 2′-bipyridine is μ_2-$\eta_N^1\eta_N^1$. Ag clusters are anionic clusters with -1 valence and consist of ten silver ions and eleven iodide ions as shown Fig. 2b. In which, Ag1 is coordinated by four μ_4-I (I1, I1#1, I2, I2#1) to form a tetrahedral configuration. Ag2 is coordinated by a μ_2-I (I4), a μ_3-I (I3) and a μ_4-I (I4) to form a deformed triangular pyramid configuration. Ag3 is coordinated by one μ_2-I

Fig. 1 Compound **1**: **a** the coordination environment of metal Co; **b** the coordination environment of metal Ag; **c** the connection mode of ligand phen; **d** 1D chain structure; **e** 2D layered structure; **f** 2D layered structure
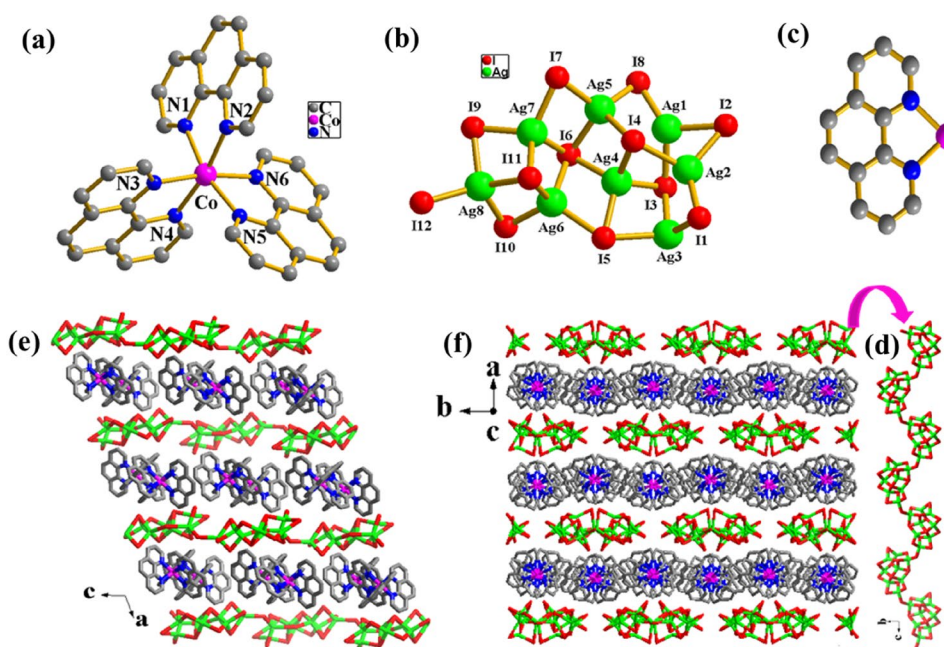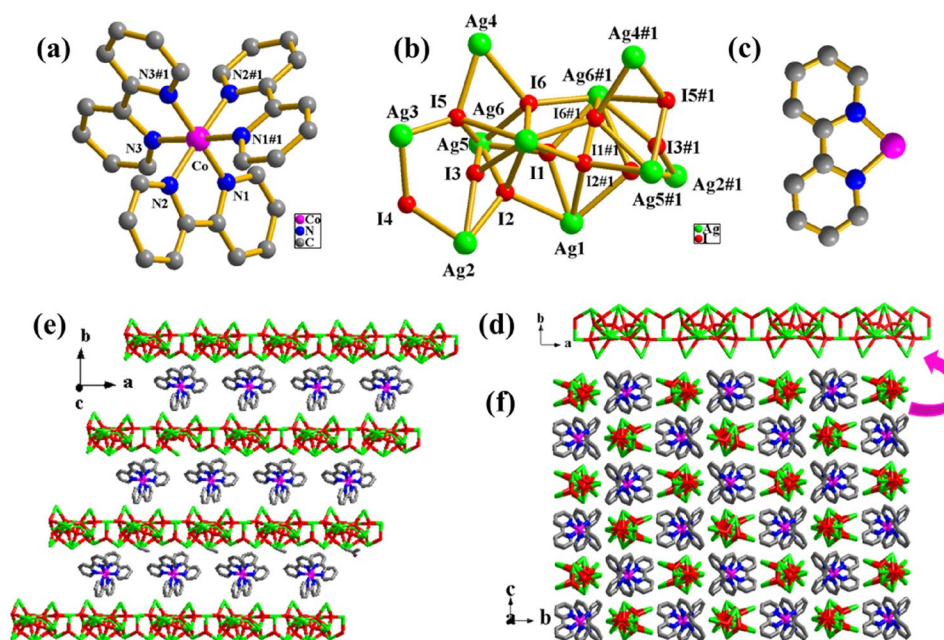

Fig. 2 Compound **2**: **a** The coordination environment of metal Co; **b** The coordination environment of metal Ag; **c** The connection of ligand 2, 2′-bipy; **d** 1D chain structure; **e** 2D layered structure (#1: 1-x, y, 0.5-z); **f** 2D layered structure (#1: 1-x, y, 0.5-z)

(I4) and two μ_3-I (I5, I5#1) to form a triangular pyramid configuration. Ag4 is coordinated by a μ_2-I (I4) and a μ_4-I (I6) to form a V shape. Ag5 is coordinated by one μ_3-I (I3) and six μ_4-I (I1, I1#1, I2, I5, I6, I6#1) to form a deformed pentagonal biconical configuration. Ag6 is coordinated by one μ_3-I (I3) and four μ_4-I (I1, I2, I5, I6) to form a triangular double cone configuration. The coordination environment of metallic Ag ions is shown in Table S6. The bond length range of Ag-I bond in compound **2** is 2.736–3.212 Å, which is similar to the bond length range of Ag-I bond (2.737–3.181 Å) reported in the literatures [46–48]. Two V shaped AgI$_2$, three

triangular pyramid configuration AgI$_3$, one tetrahedral configuration AgI$_4$, two triangular biconical configuration AgI$_5$ and two deformed pentagonal biconical configuration AgI$_7$ are connected by the sharing edges to form a "kite Shaped" Ag$_{10}$I$_{11}$ building block. As shown in Fig. 2d, the building blocks are connected by shared edges Ag3–I4 to form a one-dimensional chain structure. Similarly, like the structure of **1**, as shown in Fig. 2e and 2f, a more stable interlaced layered super molecular structure is formed between the metal Ag cluster part and the metal Co cluster part through the electrostatic interaction between the anion and the cation.

3.6 Electrochemical Properties of 1 and 2

Figure 3 is the CV curve of carbon paste electrode and compounds **1** and **2** electrode in NaOH electrolyte solution. Compared with the carbon paste electrode, the redox peak of **1** and **2** appeared. Figure 3a is the CV curve of **1**, The oxidation peak is at 0.276 V and its current value is 2.696×10^{-7} A; the reduction peak is at − 0.015 V and its current value is -2.407×10^{-7} A. Figure 3b is the CV curve of **2**. The oxidation potential is at 0.261 V and the current value is 8.018×10^{-6} A; the reduction potential is at 0.039 V and the current value is -1.347×10^{-5} A. According to Eq. 1, it can be detected whether the electrode reaction is Nernst reaction. When $T = 298$ K, it can be simplified to $\Delta Ep = 59/z$. When the value of ΔEp is close to $59/z$, the electrode reaction is a reversible reaction. The ΔEp value of **1** is 251 mV, the ΔEp value of **2** is 222 mV, and its ΔEp value cannot be close to $59/z$, so the electrode reactions of **1** and **2** are all irreversible reactions. In an irreversible reaction, the number of transferred electrons in the oxidation process can be calculated by Eq. 2. According to Eq. 1, the number of transferred electrons of **1** and **2** is calculated to be 1.5 and 1.5, respectively. Therefore, the compounds **1** and **2** transfer 1.5 electrons during the oxidation process.

$$\Delta Ep = 2.3RT/zF \tag{1}$$

$$|Ep - Ep/2| = 47.7/(1 - \alpha)n \tag{2}$$

where ΔEp is the difference between oxidation potential and reduction potential (mV), R is 8.314 J/(mol K), T is temperature (K), z is the number of transferred electrons, F is 96500 C/mol, Ep is the oxidation peak Potential (mV), $Ep/2$ is the half-peak potential (mV), α is the electron transfer coefficient, which is approximately 0.5, and n is the number of transferred electrons.
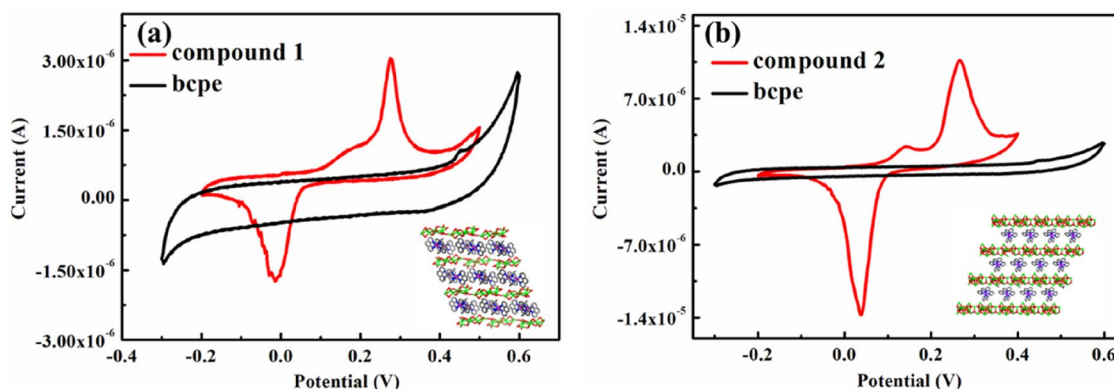
3.6.1 The Influence of Different Scanning Speed on Cyclic Voltammetry

By studying the CV curves of **1** and **2** at different scan rates, the CV curve at the best scan rate was determined. It can be seen from Fig. 4 that with the increase of the sweep rate, the peak current of the reduction potential and the oxidation potential of **1** first increase to the maximum and then decrease. At a sweep rate of 0.05 V/s, the peak current of **1** reaches the maximum and the peak shape is complete. Therefore, the best sweep speed of the CV curve of **1** is 0.05 V/s. Figure 5a and Fig. 5b are the CV curves of **2** at different sweep speeds. It can be seen from the figure that the reduction potential and the peak current of the oxidation potential of **2** increase with the increase of the sweep rate. When the sweep speed is 0.1 V/s, the peak current reaches the maximum and the peak shape is complete. Therefore, the best sweep rate for the CV curve of **2** is 0.1 V/s.

3.6.2 The Influence of Different Resting Time on Cyclic Voltammetry

Through the research on the CV curve of **1** and **2** under different resting time, the CV curve under the best resting time is determined. It can be seen from Fig. 6 that the peak currents of the oxidation potential and reduction potential of **1** gradually decrease and then almost remain unchanged when the resting time increases. When the rest time is equal to 5 s, the peak current of the CV curve of **1** reaches the maximum and the peak shape is complete. Therefore, the optimal resting time of the CV curve of **1** is 5 s. It can be seen from Fig. 7 that as the sweep rate increases, the peak current of **2** also decreases, and remains unchanged after decreasing to the minimum. When the sweep speed is 5 s, the peak current reaches the maximum and the peak shape is perfect. Therefore, the optimal resting time of the CV curve of **2** is 5 s.
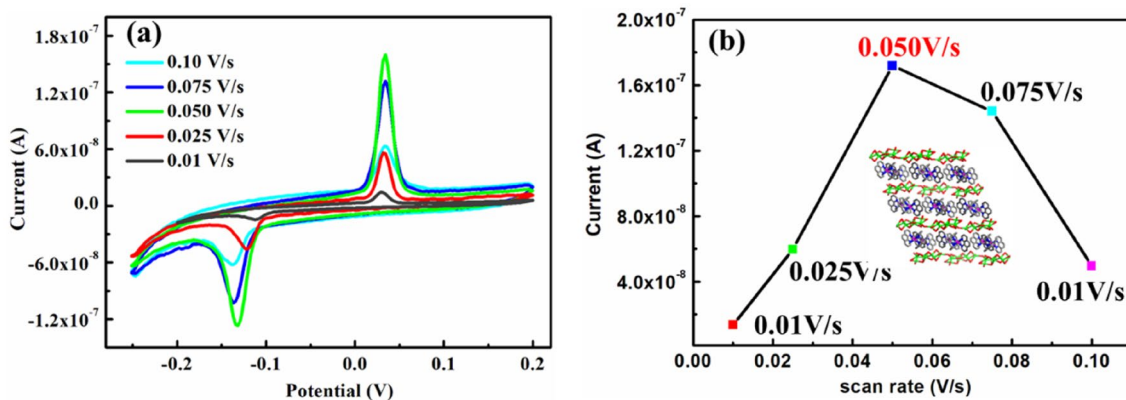

Fig. 3 CV curves of bcpe and **1** and **2**

Fig. 4 **a** CV curves of **1** at different scan rates; **b** the line chart of peak current at different scan rates of **1**
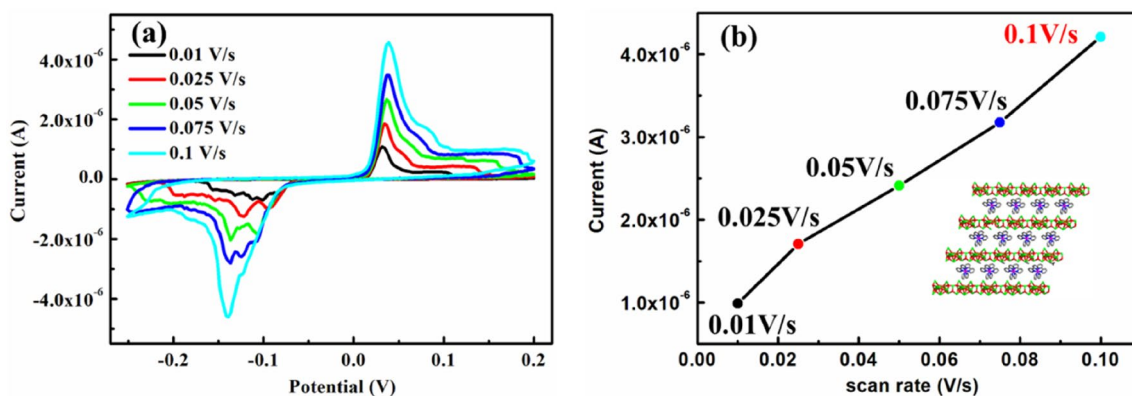

Fig. 5 **a** CV curves of **2** at different scan rates; **b** the line chart of peak current at different scan rates of **2**
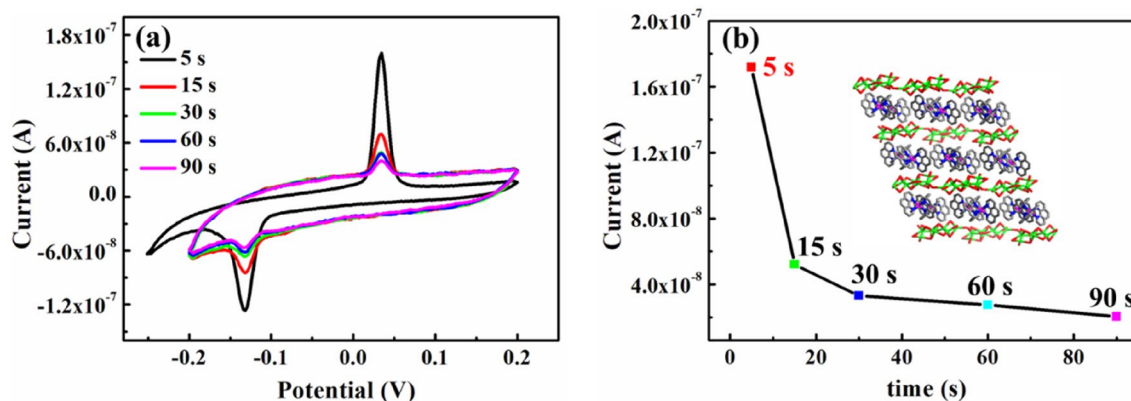

Fig. 6 **a** CV curves of **1** at different time; **b** the line chart of peak current at different time of **1**

3.6.3 The Influence of Different pH on Cyclic Voltammetry Curve

The CV curves of **1** and **2** were tested under the condition of phosphate buffer solution of different pH to study the effect of pH on the CV curves of **1** and **2**. It can be seen from Fig. 8 that as the pH changes from 5 to 6, the peak current of the reduction potential and oxidation potential of **1** reaches the maximum; as the pH changes from 6 to 8, the peak current gradually decreases. Therefore, pH = 6 can be used as

the optimal pH for the CV curve of **1**. It can be seen from Fig. 9 that with the increase of pH, the peak current of **2** also increases, increases to the maximum and then decreases. When the pH is 8, the peak current reaches the maximum and the peak shape is good. Therefore, the optimal pH of the CV curve of **2** is 8.
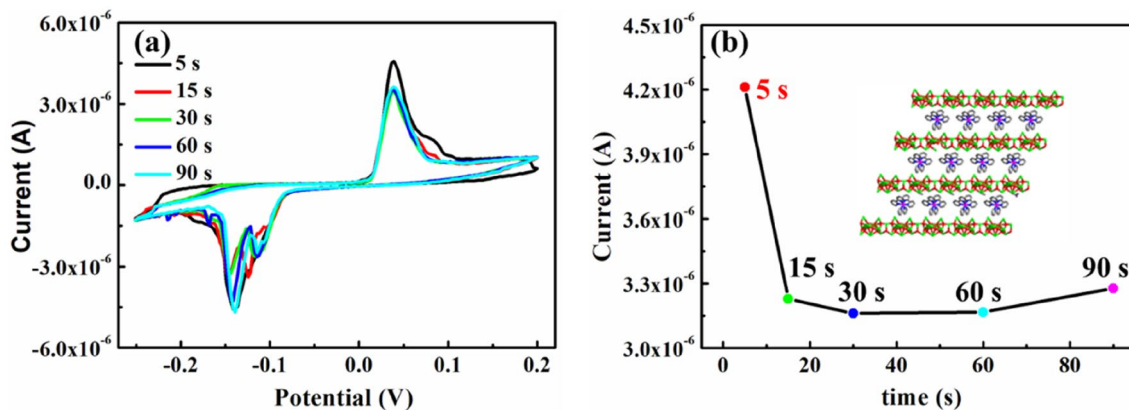

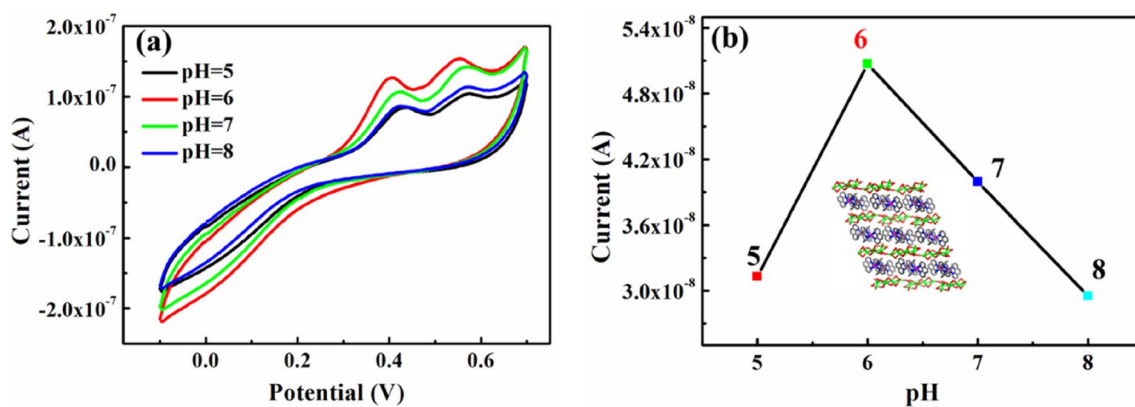**Fig. 7** **a** CV curves of **2** at different time; **b** the line chart of peak current at different time of **2**

Fig. 8 **a** CV curves of **1** at different pH; **b** the line chart of peak current at different pH of **1**
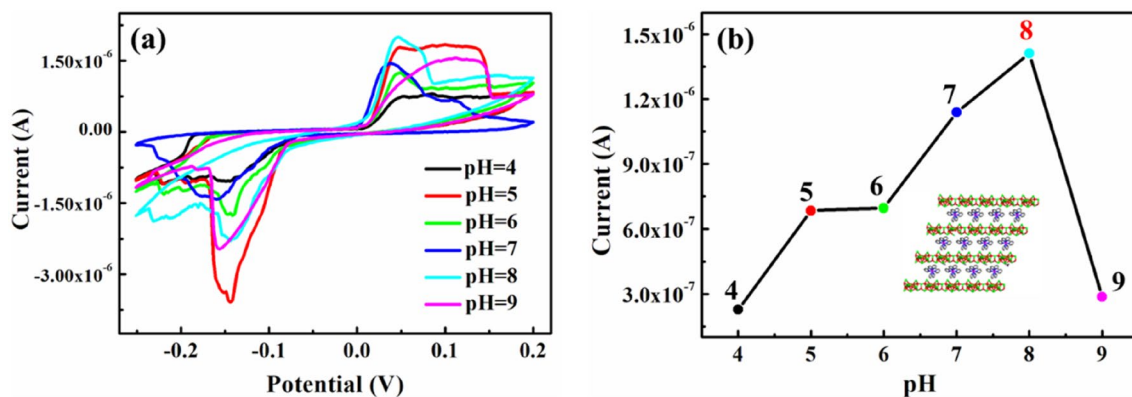

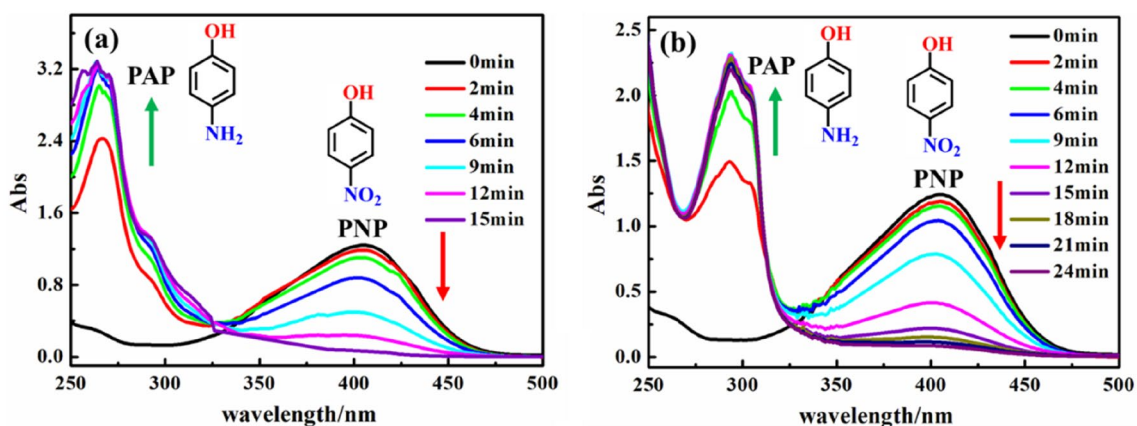**Fig. 9** **a** CV curves of **2** at different pH; **b** the line chart of peak current at different pH of **2**

Fig. 10 Curves of catalytic reduction of PNP: **a 1**; **b 2**

3.7 Catalytic Reduction of PNP by 1 and 2

After adding NaBH$_4$ to the PNP solution, the color changed to bright yellow and a characteristic peak appeared at 400 nm. This is because PNP is ionized under alkaline conditions, and a large amount of H$^+$ are released under the

condition of the catalyst, and PNP is catalytically reduced to PAP. The characteristic absorption peak of PAP is at 298 nm. As shown in Fig. 10, as time increases, the characteristic peak at 400 nm gradually decreases, while the characteristic peak at 298 nm gradually increases. This means that the concentration of PNP is gradually decreasing, and the
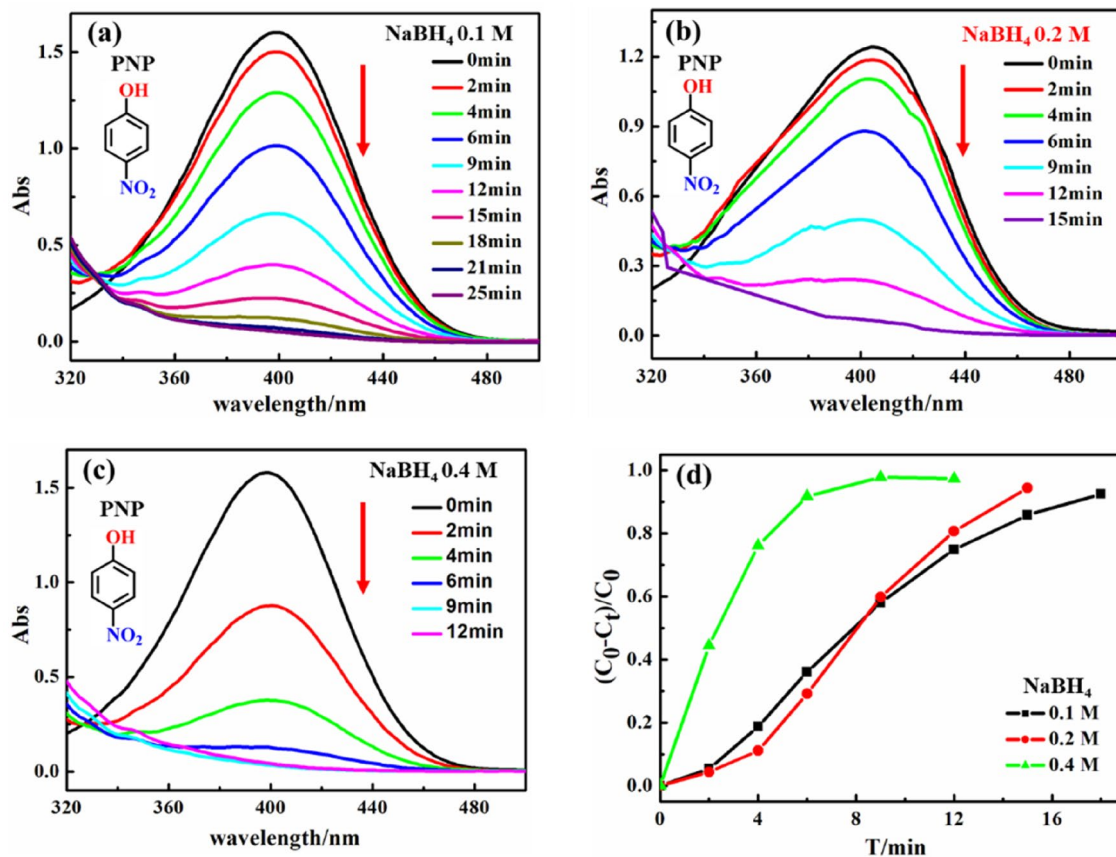

Fig. 11 Effect of NaBH$_4$ concentration on catalytic reduction of PNP with **1**: **a** 0.1 M; **b** 0.2 M; **c** 0.4 M; **d** Comparison of removal rates

concentration of PAP is increasing. It can be seen that PNP is catalytically reduced to PAP under the combined action of **1** and **2** and NaBH$_4$, and the reduction rates of **1** and **2** can reach more than 90%.

3.7.1 The Effect of Different Concentrations of Sodium Borohydride

Because NaBH$_4$ is a key parameter that controls the entire redox reaction, it is necessary to determine the optimal concentration of NaBH$_4$. A series of catalytic reduction experiments were carried out under the conditions of NaBH$_4$ concentration of 0.1–0.4 M, PNP concentration of 0.1 mM and 5 mg of the compound. As shown in Fig. 11, when the NaBH$_4$ concentrations were 0.1 M, 0.2 M, and 0.4 M, the removal rates of PNP by the catalytic reduction of **1** were 95.7%, 94.4% and 97.4%, respectively. As the concentration of NaBH$_4$ increases, the removal rate of catalytic reduction of PNP does not change significantly. Taking into account the length of the reduction time, the optimal concentration of NaBH$_4$ for the catalytic reduction of PNP in **1** was determined to be 0.2 M. As shown in Fig. 12, when the NaBH$_4$

concentration is 0.1 M, 0.2 M, and 0.4 M, the removal rate of PNP by the catalytic reduction of **2** is 30.1%, 92.9%, and 99.3%, respectively. As the concentration of NaBH$_4$ increases, the removal rate of catalytic reduction PNP also increases, but the removal rate of 0.2 M and 0.4 M NaBH$_4$ does not change much. Taking into account the utilization of the compound, the optimal concentration of NaBH$_4$ for the catalytic reduction of PNP in **2** was determined to be 0.2 M.

3.7.2 The Effect of Different Concentrations of PNP

In order to determine the optimal concentration of PNP in the catalytic reduction process, a series of catalytic reduction experiments were carried out under the condition that the NaBH$_4$ concentration was 0.2 M and the 5 mg compound was unchanged. As shown in Fig. 13, when the PNP concentrations were 0.05 mM, 0.1 mM, and 0.15 mM, the removal rate of PNP by the catalytic reduction of **1** was 97.0%, 94.4%, and 90.1%, respectively. As the PNP concentration increases, the removal rate of catalytic reduction PNP decreases, but the removal rate does not change much. The time for catalytic reduction of 0.15 mM PNP
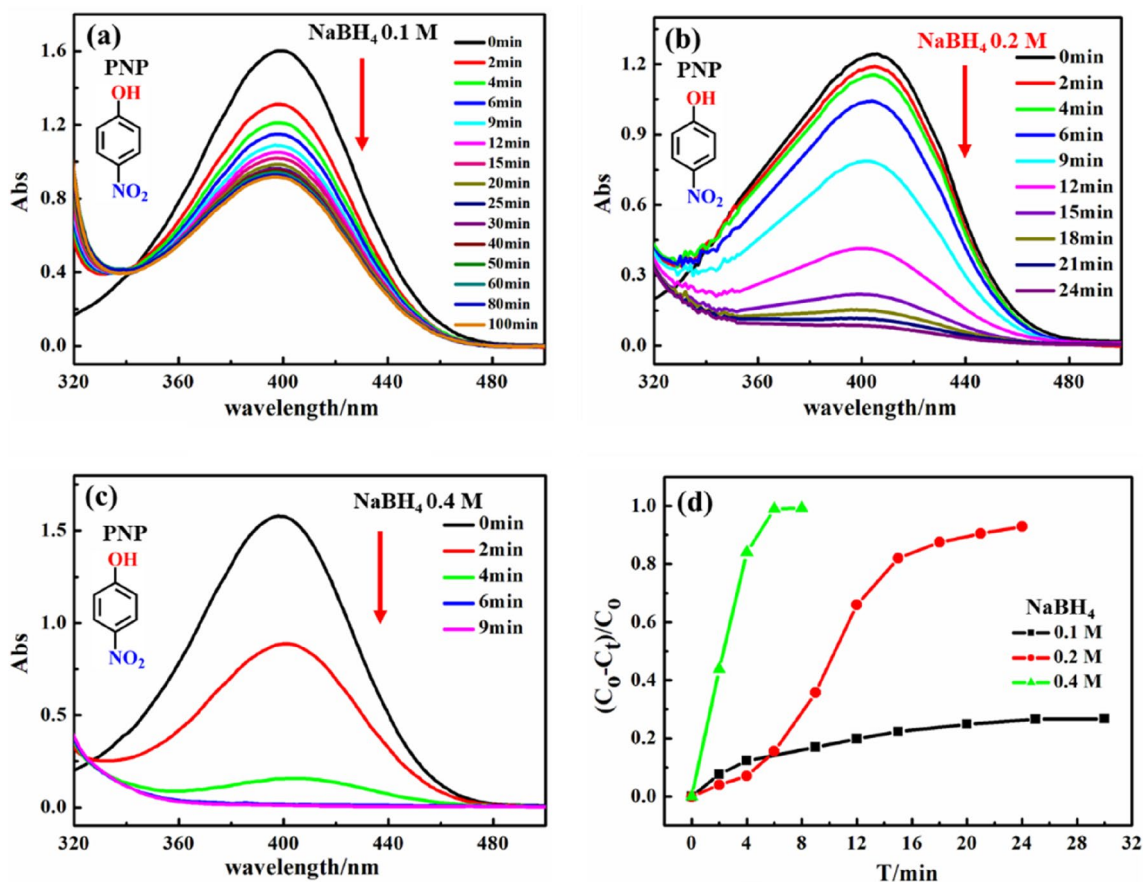

Fig. 12 Effect of NaBH$_4$ concentration on catalytic reduction of PNP with **2**: **a** 0.1 M; **b** 0.2 M; **c** 0.4 M; **d** Comparison of removal rates
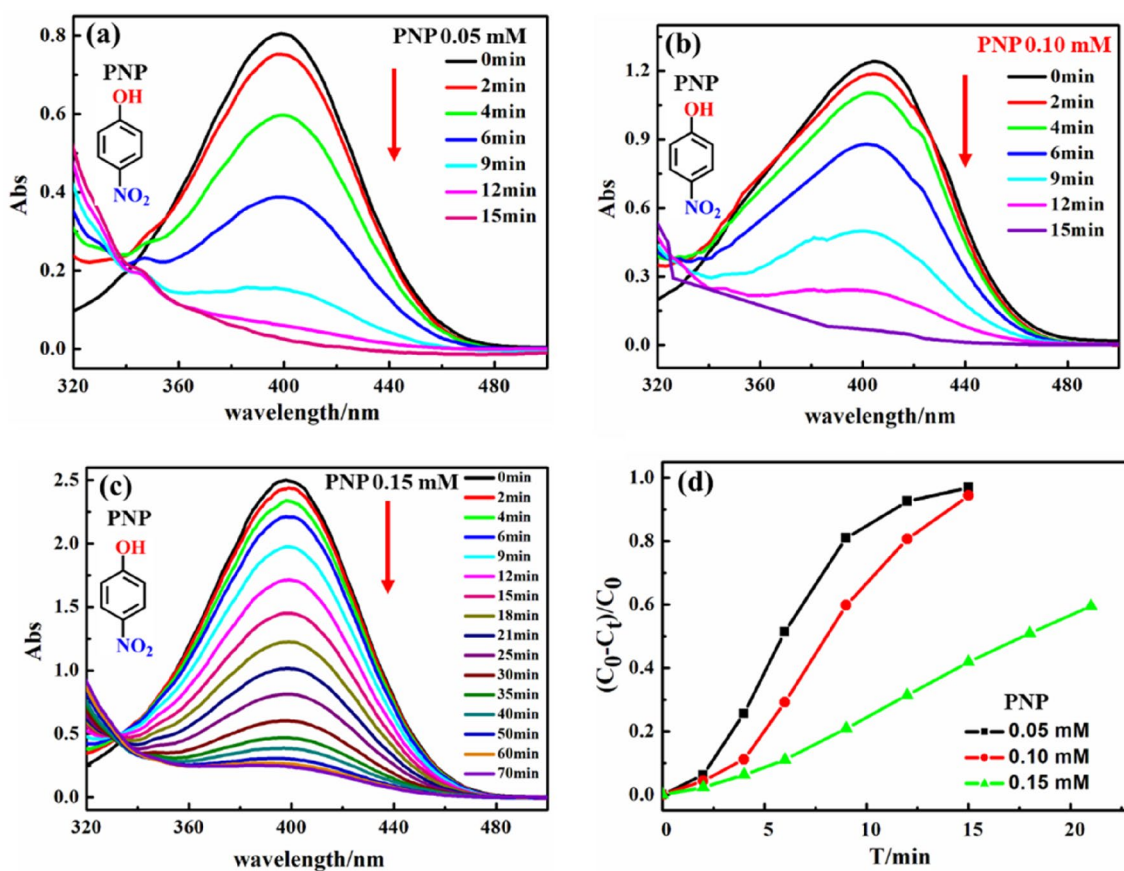
Fig. 13 Effect of PNP concentration on catalytic reduction of PNP with **1**: **a** 0.05 mM; **b** 0.1 mM; **c** 0.15 mM; **d** Comparison of removal rates

solution of **1** is 70 min, which is relatively long, while the time for catalytic reduction of both 0.05 mM and 0.1 mM PNP solutions is 15 min. Taking into account the length of the reduction time and the utilization of the compound, the optimal PNP concentration for the catalytic reduction of **1** was determined to be 0.1 mM. As shown in Fig. 14, when the PNP concentration is 0.05 mM, 0.1 mM, and 0.15 mM, the removal rate of PNP by the catalytic reduction of **2** is 100%, 92.9%, and 62.8%, respectively. With the increase of PNP concentration, the removal rate of PNP by the catalytic reduction of **2** decreases. When **2** is used for catalytic reduction of 0.05 mM PNP solution, the reduction time is 2 min, which does not make full use of the compound. When catalytic reduction of 0.15 mM PNP solution, the reduction time is longer and the reduction rate is lower. Taking into account the utilization of the compound and the reduction removal rate, the optimal PNP concentration for the catalytic reduction of **2** was determined to be 0.1 mM.

3.7.3 The Influence of the Amount of Different Catalysts

In order to make full use of the reducibility of the compound, the optimal dosage of the compound in the catalytic reduction of PNP was determined. A series of catalytic reduction experiments were carried out under constant conditions of $NaBH_4$ concentration of 0.2 M and PNP concentration of 0.1 mM. As shown in Fig. 15, in the case of 3 mg, 5 mg, and 10 mg of **1**, the removal rates of catalytic reduction of PNP are 83.4%, 94.4%, and 97.7%, respectively. With the increase of the amount of **1**, the removal rate of catalytic reduction PNP increases, but the degree of removal rate changes little. Taking into account the length of the reduction time and the utilization of the compound, the optimal dosage of **1** was determined to be 5 mg. As shown in Fig. 16, in the case of 3 mg, 5 mg, and 10 mg of **2**, the removal rate of PNP by the catalytic reduction of **2** is 48.6%, 92.9%, and 100%, respectively. As the amount of **2** increases, the removal rate
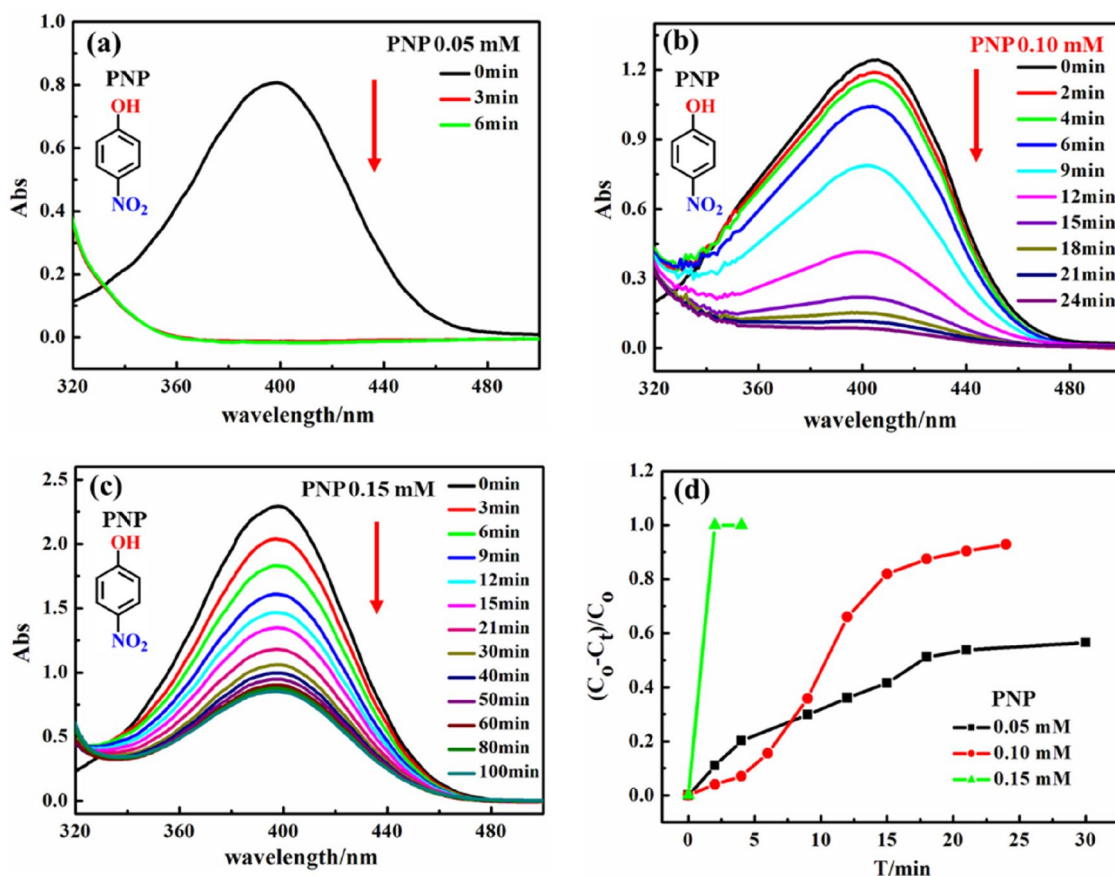
Fig. 14 Effect of PNP concentration on catalytic reduction of PNP with **2**: **a** 0.05 mM; **b** 0.1 mM; **c** 0.15 mM; **d** comparison of removal rates

of catalytic reduction of PNP increases. When 10 mg of **2** is used for catalytic reduction of PNP solution, the reduction time is very short, and it is useless to make full use of the compound. When 3 mg of **2** is used for catalytic reduction of PNP solution, the reduction time is longer and the reduction rate is lower.

Therefore, considering the utilization and reduction rate of the compound, the optimal dosage of **2** was determined to be 5 mg.

3.8 Kinetic Study of Catalytic Reduction Process

In order to analyze the kinetic behavior of the catalytic reduction of PNP solution by **1** and **2**, we used the quasi-first-order kinetic Eq. 3 and the quasi-second-order kinetic Eq. 4 to linearly fit the catalytic reduction process of PNP, and we obtained Fig. 17 and other related parameters Table 1.

$$\ln \left(C_t / C_0 \right) = -k_1 t \tag{3}$$

$$1/C_t - 1/C_0 = k_2 t \tag{4}$$

where C_e (mol/L) represents the equilibrium concentration, C_t (mol/L) represents the concentration at a certain moment, k_1 (min^{-1}) and k_2 (L/(mol/min)) represent the rate constant respectively, t (min) Is the reaction time.

It can be seen from Fig. 17 that the R^2 values of the pseudo-first-order kinetic equation fitted by the catalytic reduction of PNP by **1** and **2** are 0.9952 and 0.9901, respectively, which are closer to 1 than the R^2 value of the pseudo-second-order kinetic equation. This indicates that the catalytic reduction of PNP solution by **1** and **2** conforms to the quasi-first order kinetic model.

3.9 Study on the Mechanism of Catalytic Reduction of PNP

In order to better understand the process of the catalytic reduction of PNP solution by **1** and **2**, we speculated on the mechanism of the catalytic reduction process. It can be seen
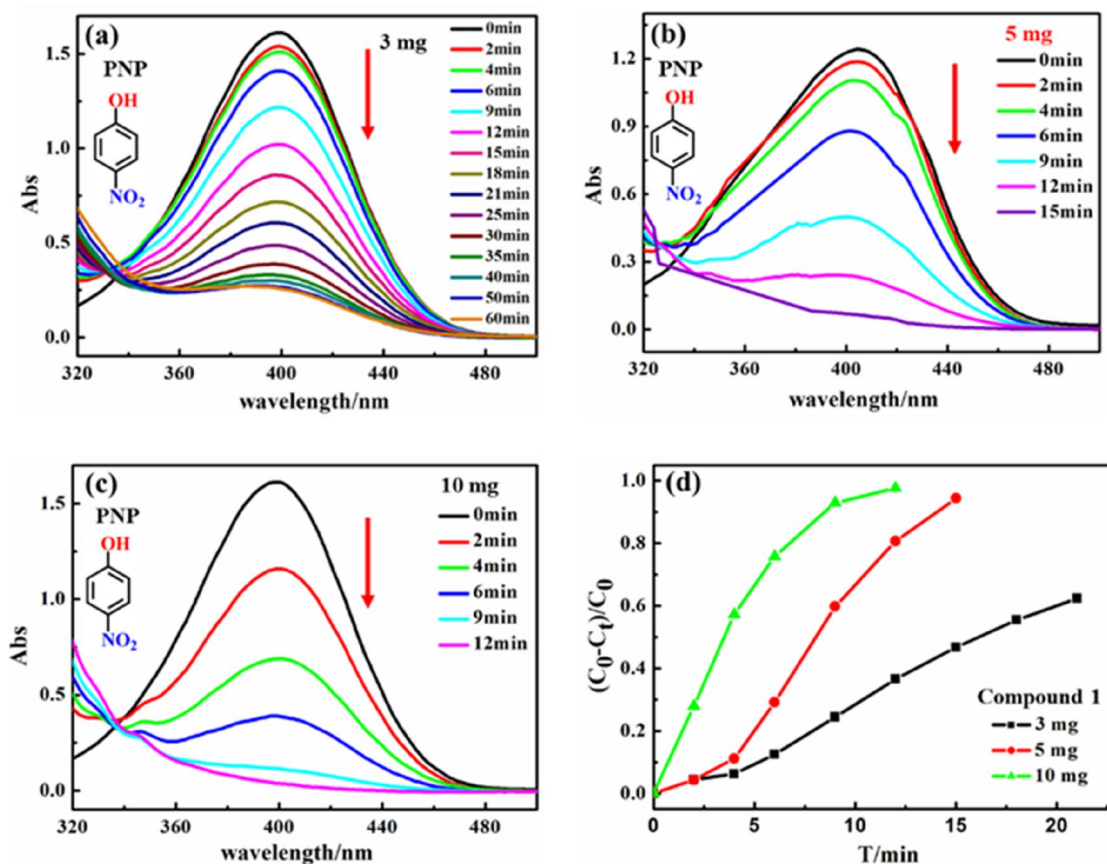
Fig. 15 Effect of compound dose on catalytic reduction of PNP with **1**: **a** 3 mg; **b** 5 mg; **c** 10 mg; **d** comparison of removal rates of PNP in catalytic reduction of **1** with compound dose

from the above that the compounds **1** and **2** exhibits good redox properties. Therefore, the mechanism of the catalytic reduction of PNP by **1** and **2** is: (i) The compounds 1 and 2 oxidize BH_4^- to BO_2^- and release H^+. The reaction energy barrier is greatly reduced. The rapid transfer of electrons correspondingly increases the surface potential difference between the compounds, which increases oxidize BH_4^- by compounds, the H^+ released by BH_4^- can catalyze PNP and accelerates the reaction rate [49]. It becomes a PAP solution and emits hydrogen gas (Fig. 18).

4 Conclusions

This work uses solvent evaporation method to design and synthesize two silver cluster compounds $\{[Co(1,10'-phen)_3]_2 \cdot [Ag_8I_{12}]\}$ (**1**) and $\{[Co(2,$ $2'-bipy)_3] \cdot [Ag_{10}I_{11}] \cdot (OH) \cdot 3DMF \cdot 2H_2O\}$ (**2**). The compounds **1** and **2** form an infinite two-dimensional planar structure through the electrostatic interaction between anion and cation. Compounds **1** and **2** can efficiently catalytically reduce PNP in aqueous solution, and the reduction removal rate can reach more than 90%. At the same time, kinetic analysis showed that the catalytic reduction of PNP by **1** and **2** fits well with the quasi-first-order kinetic model. The redox properties of **1** and **2** were determined by cyclic voltammetry curve. Therefore, the mechanism of the catalytic reduction of PNP by **1** and **2** is that the silver cluster anion in **1** and **2** deoxidizes BH_4^- through its own oxidative property and releases H^+, and then H^+ catalytically reduces PNP to PAP, which releases hydrogen. Therefore, the compounds **1** and **2** can be used as a reducing agent for efficiently removing PNP in aqueous solution, and has good application prospects.
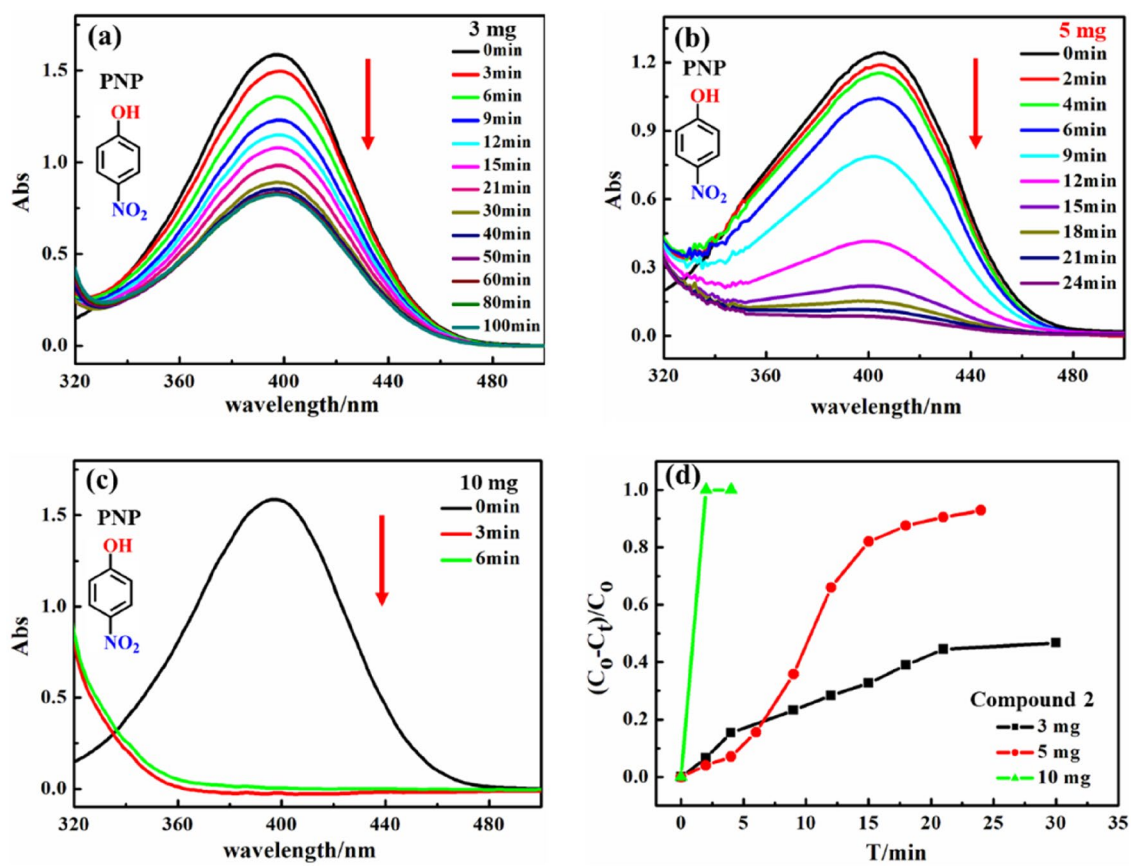
Fig. 16 Effect of compound dose on catalytic reduction of PNP with **2**: **a** 3 mg; **b** 5 mg; **c** 10 mg; **d** comparison of removal rates of PNP in catalytic reduction of **2** with compound dose
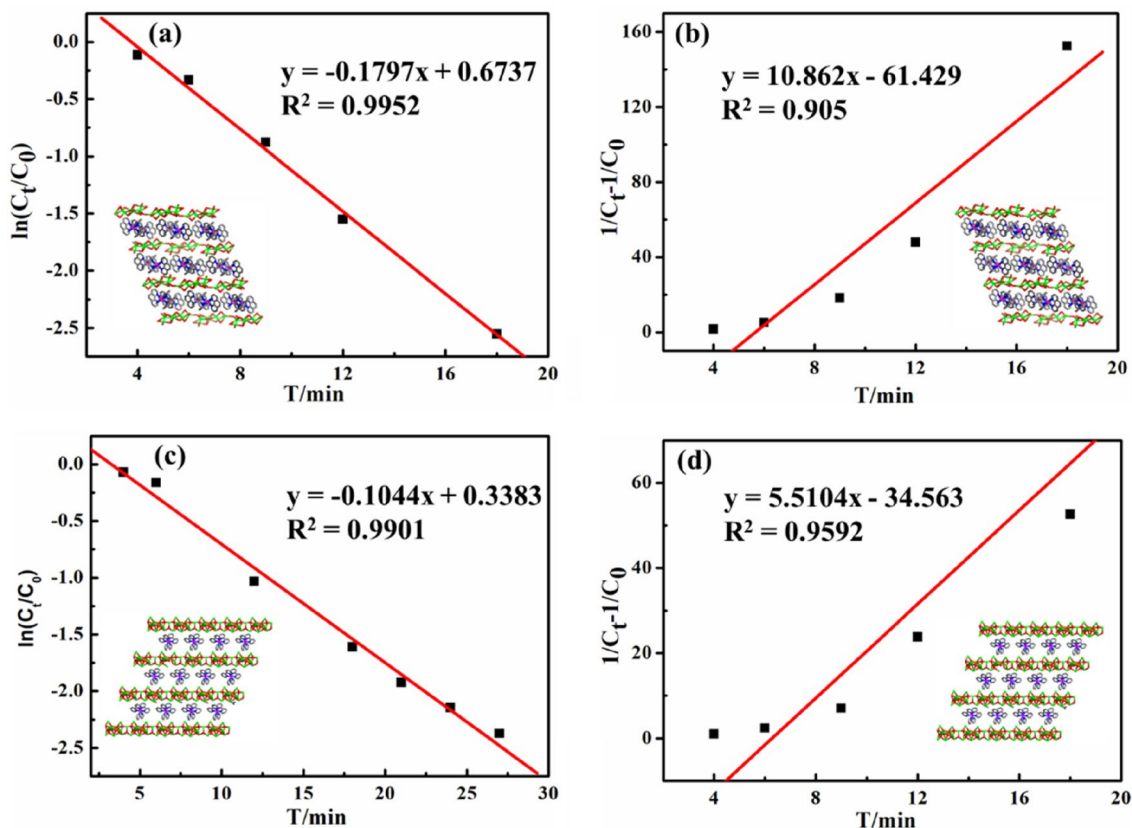
Fig. 17 a Pseudo-first-order kinetic curves of catalytic reduction of PNP with **1**; **b** pseudo-second-order kinetic curves of catalytic reduction of PNP with **1**; **c** pseudo-first-order kinetic curves of catalytic reduction of PNP with **2**; d pseudo-second-order kinetic curves of catalytic reduction of PNP with **2**

Table 1 Correlation data of pseudo-first-order and pseudo-second-order kinetics

Compounds	Pseudo first-order kinetics model		Pseudo secondary-order kinetics model	
	k_1 (min^{-1})	R^2	k_2 (g/(mg·min))	R^2
1	0.1797	0.9952	10.862	0.905
2	0.1044	0.9901	5.5104	0.9592
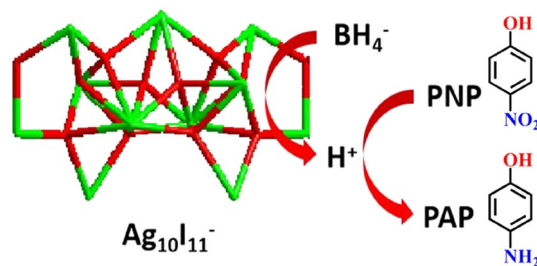
Fig. 18 Mechanism of catalytic reduction of PNP

Author Contributions Min Liu, experiment, process data, writing; Yu Xin, reviewing; Yong Heng Xing, reviewing and editing, supervision; Feng Ying Bai, reviewing and editing, supervision; Zhan Shi, software.

Declarations

Conflict of interest There are no conflicts to declare.

References

1. P. Yang, T.T. Nie, J. Hu, H.Q. Ni, J.J. Shi, Funct Mater. Lett. **13**, 1950091–3 (2020)
2. L. Tan, A.D. Tang, Y. Zou, M. Long, Y. Zhang, J.O. Yang, J. Chen, Sci. Rep. **7**, 3281–11 (2017)
3. T.H. Zhao, F.H. Zhang, J. Zhou, X.Q. Zhao, Comments Inorg. Chem. **41**, 1–33 (2020)
4. P.P. Guo, M. Liu, L.L. Shi, J. Solid State Chem. **286**, 121247–121325 (2020)
5. H.A. Alidağı, S.O. Tümay, A. Şenocak, S. Yeşilot, Dyes Pigm. **153**, 172–181 (2018)
6. Z.M. Shammi, A.H. Kianfar, M.M. Momeni, J. Mater. Sci. Mater. Electron. **31**, 14810–14822 (2020)
7. Y. Gu, Y.Q. Jiao, A.P. Wu, X.G. Zhou, B. Buhe, T.W. Yin, B.J. Jiang, Y. Qu, C.G. Tian, Res. Chem. Intermed. **43**, 4759–4779 (2017)
8. S. Alghool, H.F. Abd El-Halim, A.M. Mostafa, J. Inorg. Organomet. Polym. Mater. **29**, 1324–1330 (2019)
9. C. Paun, G. Słowik, E. Lewin, J. Sá, RSC Adv. **6**, 87564–87568 (2016)
10. J. Feng, Q. Wang, D.L. Fan, L.R. Ma, D.L. Jiang, J.M. Xie, J.J. Zhu, Appl. Surf. Sci. **382**, 135–143 (2016)
11. U.A. Sánchez, L.F. Chen, J.A. Wang, L.E. Noreña, M. Asomoza, S. Solis, X.L. Zhou, Y.Q. Song, J. Liu, Int. J. Photoenergy **2019**, 1–13 (2019)
12. T. Liu, N. Chen, Y. Deng, F.X. Chen, C.P. Feng, RSC Adv. **10**, 15901–15912 (2020)
13. G. Eshaq, S.B. Wang, H.Q. Sun, M. Sillanpaa, J. Hazard. Mater. **382**, 121059–121145 (2020)
14. W.M. Zhang, Z.W. Zhou, X.Y. Shan, R. Xu, Q. Chen, G.Y. He, X.Q. Sun, H.Q. Chen, New J. Chem. **40**, 4769–4774 (2016)
15. J.Y. Du, Y. Zhao, J. Chen, P. Zhang, L.L. Gao, M.Q. Wang, C. Cao, W. Wen, C.Q. Zhu, RSC Adv. **7**, 33929–33936 (2017)
16. J.W. Sun, J.S. Xu, A. Grafmueller, X. Huang, C. Liedel, G. Algara-Siller, M. Willinger, C. Yang, Y.S. Fu, X. Wang, M. Shalom, Appl. Catal. B **205**, 1–10 (2017)
17. J.S. Wu, J.S. Wang, T.N. Wang, L.M. Sun, Y.C. Du, Y.L. Li, H.Y. Li, Appl. Surf. Sci. **466**, 342–351 (2019)
18. G. Shimoga, R.R. Palem, S.H. Lee, S.Y. Kim, Metals **10**, 1661–1720 (2020)
19. A.R. Zeng, A.R. Zeng, Water Air Soil Pollut. **8**, 278–287 (2017)
20. M. Lei, W. Wu, S.L. Yang, X.G. Zhang, Z. Xing, F. Ren, X.H. Xiao, C.Z. Jiang, Part. Part. Syst. Charact. **33**, 212–220 (2016)
21. T.L. Guo, C. Wang, N.N. Zhang, Y. Zhang, T. Chen, X. Xing, Z.D. Lu, L.L. Wen, Cryst. Growth Des. **9**, 6217–6225 (2020)
22. Y. Chen, X.L. Chi, Y.C. Xu, X.C. Wang, D.R. Xiao, Z. Anorg. Allg. Chem. **642**, 128–133 (2016)
23. S.X. Zhao, J.S. Wu, W.Z. Chen, J. Organomet. Chem. **848**, 249–280 (2017)
24. K. Laxman, A. Kumar, M. Ravikanth, Asian J. Org. Chem. **9**, 162–180 (2020)
25. R. Lopes, Á. Raya-Barón, M.P. Robalo, C. Vinagreiro, S. Barroso, M.J. Romão, L. Fernández, M.M. Pereira, B. Royo, Eur. J. Inorg. Chem. **2021**, 22–29 (2020)
26. P. Sánchez, M. Hernández-Juárez, N. Rendón, J. López-Serrano, L.L. Santos, E. Álvarez, M. Paneque, A. Suárez, Dalton Trans. **49**, 9583–9587 (2020)
27. W.S. Ouyang, J.H. Rao, Y.B. Li, X.H. Liu, Y.P. Huo, Q. Chen, X.W. Li, Adv. Synth. Catal. **362**, 5576–5600 (2020)
28. F.X. Cheng, S.W. Yu, M.L. Ren, C.X. He, H.J. Yin, Transit. Met. Chem. **41**, 305–314 (2016)
29. N.S. Bedowr, R.B. Yahya, N. Farhan, J. Saudi Chem. Soc. **22**, 255–260 (2018)
30. S.A. Elsayed, E.A. Gaml, M.A. Nasher, Opt. Mater. **84**, 8–15 (2018)
31. T.J. Greenfield, M.M. Turnbull, J. Zubieta, R.P. Doyle, Inorg. Chim. Acta **498**, 119084–119094 (2019)
32. Z.N. Gafurov, A.B. Dobrynin, I.F. Sakhapov, A.A. Kagilev, A.O. Kantyukov, A.A. Balabaev, A.V. Toropchina, O.G. Sinyashin, D.G. Yakhvarov, Phosphorus Sulfur Silicon Relat. Elem. **194**, 517–521 (2019)
33. L. Lu, X.Q. An, W.X. Huang, Anal. Methods **9**, 23–27 (2017)
34. R.W. Huang, Y.S. Wei, X.Y. Dong, X.H. Wu, C.X. Du, S.Q. Zang, T.C.W. Mak, Nat. Chem. **9**, 689–697 (2017)
35. X.X. Liang, S.X. Luan, Z.Q. Yin, M. He, C.L. He, L.Z. Yin, Y.F. Zou, Z.X. Yuan, L.X. Li, X. Song, C. Lv, W. Zhang, Eur. J. Med. Chem. **157**, 62–80 (2018)
36. L.B. Wang, H. Chen, Q.Y. Yin, J. Kang, B. Liu, G.S. Weng, J. He, Nanotechnology **31**, 245703–245714 (2020)
37. Y. Mu, D. Wang, X.D. Meng, J. Pan, S.D. Han, Z.Z. Xue, Cryst. Growth Des. **20**, 1130–1138 (2020)
38. Z.Z. Xue, X.D. Meng, X.Y. Li, S.D. Han, J. Pan, G.M. Wang, Inorg. Chem. **60**, 4375–4379 (2021)
39. J. Zheng, J.N. Wang, T. Wang, K. Wu, R.J. Wei, W.G. Lu, D. Li, J. Phys. Chem. C. **125**, 9400–9410 (2021)
40. C.Y. Tang, J. Yao, Y.Y. Li, Z.R. Xia, J.B. Liu, C.Y. Zhang, Inorg. Chem. **59**, 13962–13971 (2020)
41. T.S. Sunil Kumar Naik, B.E. Kumara Swamy, J. Electroanal. Chem. **826**, 23–28 (2018)
42. M. Kumar, M. Wang, B.E. Kumara Swamy, M. Praveen, W. Zhao, Colloids Surf. B **196**, 111299–41 (2020)
43. K. Chetankumar, B.E. Kumara Swamy, S.C. Sharma, Mater. Chem. Phys. **252**, 123231–34 (2020)
44. C. Wang, N. Zhang, C.Y. Hou, X.X. Han, C.H. Liu, Y.H. Xing, F.Y. Bai, L.X. Sun, Transit. Met. Chem. **45**, 423–433 (2020)
45. A. You, Y. Li, Z.M. Zhang, X.Z. Zou, J.Z. Gu, A.M. Kirillov, J.W. Chen, Y.B. Chen, J. Mol. Struct. **1145**, 339–346 (2017)
46. D.D. Yang, W.L. Xu, X.W. Cao, S.J. Zheng, J.G. He, Q. Ju, Z.L. Fang, W. Huang, Inorg. Chem. **16**, 7954–7961 (2016)
47. J.J. Shen, C.F. Zhang, T.L. Yu, L. An, Y.L. Fu, Cryst. Growth Des. **12**, 6337–6342 (2014)
48. Q. Wei, D. Wang, J. Pan, S.D. Han, G.M. Wang, Chem. Asian J. **14**, 640–646 (2019)
49. Y.W. Yang, Y.Y. Mao, B. Wang, X.W. Meng, J. Han, C. Wang, H.W. Yang, RSC Adv. **6**, 32430–32433 (2016)

Publisher's Note Springer Nature remains neutral with regard to jurisdictional claims in published maps and institutional affiliations.

Authors and Affiliations

Min Liu[1] · Yu Xin[1] · Yong Heng Xing[1] · Feng Ying Bai[1] · Zhan Shi[2]

1   College of Chemistry and Chemical Engineering, Liaoning Normal University, Dalian City 116029, People's Republic of China

2   State Key Laboratory of Inorganic Synthesis and Preparative Chemistry, College of Chemistry, Jilin University, Changchun 130012, People's Republic of China